

# Measurement and Simulation of Millimeter Wave Scattering Cross-sections from Steel-Reinforced Concrete

A.M. Hassan<sup>a</sup>, N.S. Martys<sup>a</sup>, E.J. Garboczi<sup>a</sup>, R.D. McMichael<sup>a</sup>, M.D. Stiles<sup>a</sup>, D.F. Plusquellic<sup>a</sup>, P.E. Stutzman<sup>a</sup>, S. Wang<sup>a</sup>, V. Provenzano<sup>a</sup>, J.T. Surek<sup>b</sup>, D.R. Novotny<sup>b</sup>, J.B. Coder<sup>b</sup>, M.D. Janezic<sup>b</sup>, and S. Kim<sup>b</sup>

<sup>a</sup>National Institute of Standards and Technology, Gaithersburg, MD 20899.

<sup>b</sup>National Institute of Standards and Technology, Boulder, CO 80305.

**Abstract.** Some iron oxide corrosion products exhibit antiferromagnetic magnetic resonances (AFMR) at frequencies on the order of 100 GHz at ambient temperatures. AFMR can be detected in laboratory conditions, which serves as the basis for a new non-destructive spectroscopic method for detecting early corrosion. When attempting to measure the steel corrosion in reinforced concrete in the field, the actual local rebar geometry must be taken into account. Experiments and numerical simulations have been developed at frequencies near 100 GHz to sort out these effects. The experimental setup involves a network analyzer with converter heads to up-convert the output frequency, which is then connected to a horn antenna followed by a 7.5 cm diameter polymer lens to focus the waves on the sample. Two sets of samples were studied: uniform cylindrical rods and genuine rebars with different kinds of coatings. The electromagnetic scatterings from uniform rods were calculated numerically using classical modal expansion. A finite-element electromagnetic solver was used to model more complex rebar geometry and non-uniform corrosion layers. Experimental and numerical data were compared to help quantify and understand the anticipated effect of local geometrical features on AFMR measurements.

**Keywords:** Antiferromagnetic magnetic resonance, Corrosion, Nondestructive testing, Millimeter Wave, COMSOL.

**PACS:** 76.50.+g, 75.50.Ee, 81.70.-q

## INTRODUCTION

The early detection of corrosion in steel-reinforced (rebar) structural concrete is of high importance since it can lead to savings of billions of dollars in the repair and maintenance of the transportation infrastructure [1-2]. A key technical challenge is the detection of corrosion at an early stage before cracking in the concrete starts to occur. This early detection is challenging because cracking can start to occur when the corrosion layers are only a few tens of micrometers thick [2]. Some iron oxide corrosion products exhibit antiferromagnetic magnetic resonances (AFMR) in the millimeter/THz range [3]. For example, hematite is found to exhibit an AFMR at around 190 GHz at room temperature. In the temperature range between -23 °C and -13 °C, the AFMR occurs in the W-band which covers the frequency range from 75 GHz to 110 GHz [3]. AFMR has been detected in laboratory conditions using millimeter waves, which serves as the basis for a new non-destructive spectroscopic method for detecting early corrosion [3,4]. This method is being developed in a five-year project at NIST.

In real field conditions, random geometry and topology of the corrosion products and of the surface on which they grow could introduce complications in the electromagnetic (EM) response, making the identification of AFMR more challenging. While these effects are fairly small at lower frequencies, 1 GHz to 20 GHz, these aspects of corrosion and the rebar geometry start to play a larger effect at AFMR frequencies. This work investigates, experimentally and numerically, electromagnetic scattering from rebar in air in the W-band, with and without a concrete-like cover. The research reported herein will serve as an intermediate step to eventually move to the higher frequencies where AMFRs occur at room temperature. However, both the experimental and numerical work does not consider the role of the AFMRs. Modeling the actual AFMR scattering is also deferred to future work.

## NUMERICAL SIMULATIONS

As a starting point, the complex rebar geometry is simplified and modeled as an infinite multi-layered coated conducting cylinder, with normal incidence of the electromagnetic (EM) wave. Two polarizations are considered: the TM polarization, where the electric field is parallel to the axis of the cylinder and the TE polarization, where the

electric field is perpendicular to the axis of the cylinder. Numerical solutions typically assume an excitation in the form of a plane wave [5-6]. However, practical sources typically generate a Gaussian wave. Therefore, both plane wave and Gaussian wave incidence will be investigated in this work. In the case of plane waves, the scattered fields can be calculated theoretically by expanding the fields into a series of Bessel and Hankel functions with unknown coefficients [5-6]. These unknown coefficients can be calculated by applying the boundary conditions at the surface of the metallic cylinder and at each interface between the coating layers [5-6]. In the case of Gaussian wave incidence, the incident wave is decomposed into a series of Bessel functions weighted with different weights to establish the Gaussian distribution desired [7]. Once calculated, the scattered field can be used to calculate the Back Scattered Far-field pattern (BSFFP) defined as follows:

$$\text{BSFFP} = \left| \sqrt{\rho} \lim_{\rho \rightarrow \infty} (E_{\text{scattered}}) \right| \quad (1)$$

where  $E_{\text{scattered}}$  is the scattered field from the target,  $\rho$  is the distance from the target where the scattered field is measured, and  $|\cdot|$  refers to the magnitude. Taking the limit in eq. (1) removes the distance dependence of the BSFFP, making BSFFP a function only of the spherical polar angles thus allowing an easier comparison between experiment and theory.

## EXPERIMENTAL MEASUREMENTS

An Agilent\* general-Purpose Network Analyzer (PNA) was used with converter heads (6x and 8x) to up-convert the signal to the W-band. The PNA is used to feed a pyramidal horn followed by a 7.62 cm diameter HDPE lens to focus the output beam to a waist radius  $w_0=13.5$  mm at the target location. The reflection back to the antenna is then measured in the far-field in the form of the scattering parameter  $S_{11}$  (Target), which indicates the reflected power. The distance between the target and the antenna was approximately 30 cm, which is more than 70 times the largest wavelength in the W-band. Therefore, the approximation that the experimental measurements were performed in the far-field is well justified. In addition to the measurements from the various targets, the following additional measurements were performed for calibration: (a)  $S_{11}$  without any target, denoted  $S_{11}$  (No Target), and (b)  $S_{11}$  with a 10 cm x 10 cm metal reflecting plate in place of the sample, denoted  $S_{11}$  (Metal Plate). (a) gives the background and (b) gives total reflection. The post processing of the experimental measurements was performed as follows:

$$\text{BSFFP} = \frac{\{S_{11}(\text{Target}) - S_{11}(\text{No Target})\}}{\{S_{11}(\text{Metal Plate}) - S_{11}(\text{No Target})\}} \quad (2)$$

where the measurements in both the numerator and denominator of eq. (2) were time gated to remove multiple reflections between the target and the antenna and any extraneous reflections from the experimental setup. The subtraction of  $S_{11}$  (No Target) from  $S_{11}$  (Target) was performed to extract the background scattered field from the measured total field and to remove any reflection at the horn aperture or at the lens boundary. The division by  $\{S_{11}(\text{Metal Plate}) - S_{11}(\text{No Target})\}$  was performed to normalize the target signature by the signature of total reflection and to de-convolute any antenna response.

A test case was prepared to validate the experimental setup and the numerical simulations. The case consisted of a 1.27 cm diameter metallic cylinder covered by a 0.15 cm thick PMMA tube as shown in Figure 1(a). Both the TM polarization and the TE polarization were experimentally measured. The exact test case was numerically simulated using both plane waves and Gaussian waves with the same waist radius as in the experiment ( $w_0=13.5$  mm). The simulations used a complex relative permittivity  $\epsilon_r = 2.85 - j(0.06)$  for PMMA, which is comparable to the value reported for PMMA in [8]. Figure 1(b) and Figure 1(c) show the experimental measurements and the simulations for the TM and TE polarizations, respectively. The y-axis in Figure 1(b) and Figure 1(c) shows the ratio of the back

---

\* Certain commercial equipment and/or materials are identified in this report in order to adequately specify the experimental procedure. In no case does such identification imply recommendation or endorsement by the National Institute of Standards and Technology, nor does it imply that the equipment and/or materials used are necessarily the best available for the purpose.

scattered far-field pattern from the PMMA-coated cylinder to the back scattered far-field pattern from the uncoated cylinder. Figure 1(b) and 1(c) show good agreement between the experimental measurements and the numerical simulations. In Figure 1(b), the TM experimental measurement was repeated twice. The difference between the two experimental measurements, which is a measure of experimental uncertainty, can be attributed to slight movement or misalignment of the cylinder between the two measurements. Figure 1(b) shows that repeating the experiment leads to differences comparable to the differences between the experimental measurements and the simulations. Therefore, the small mismatch between the experimental measurements and the simulations can be attributed to misalignment or wobbling of the cylinder. Therefore, Figure 1 validates the accuracy of the experimental measurements and the numerical simulations employed in this work. Figure 1 also shows that there is only a small difference between the scattered field due to a plane wave incidence and a Gaussian wave incidence at the beam waist  $w_0$  value employed in this work. Therefore, the rest of the cases in this paper will assume plane wave incidence for simplicity.

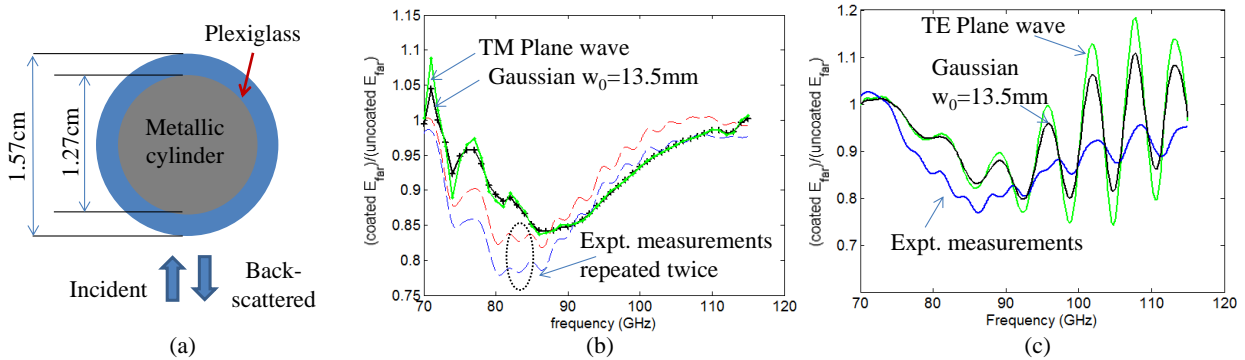


**FIGURE 1.** (a) Configuration of the test case showing the metallic cylinder covered with a PMMA tube (b) Experimental and numerical scattered fields for the TM polarization (c) Experimental and numerical scattered fields for the TE polarization.

## REBAR GEOMETRICAL FEATURES IN THE 75 GHZ-110 GHZ BAND

In this section, geometrical features of rebar in concrete will be studied using numerical simulations and/or experimental measurements. Primarily, the effect of corrosion thickness, the effect of concrete thickness, the effect of non-uniform corrosion, and the effect of rebar surface geometry are investigated in the following subsections.

### Effect of Corrosion Thickness

For the case of uniform corrosion coverage, cracking in concrete can occur as a result of corrosion layers as thin as  $3 \mu\text{m}$  to  $74 \mu\text{m}$  [2]. Therefore, in this subsection the electromagnetic scattering from corrosion layers ranging in thickness from  $3 \mu\text{m}$  to  $74 \mu\text{m}$  are investigated. Figure 2 shows a 1.27 cm diameter metallic cylinder covered by a uniform layer of magnetite, which is one of the common iron oxides corrosion products. In the 75 GHz to 110 GHz W-band, magnetite has an approximate complex relative dielectric permittivity  $\epsilon_r = 7.01 - j(0.64)$  as measured in [9]. Figure 2(b) and Figure 2(c) show the TM and TE scattering, respectively, from a cylinder covered with a magnetite layer of different thicknesses. Four different thicknesses were investigated:  $3 \mu\text{m}$ ,  $27 \mu\text{m}$ ,  $50 \mu\text{m}$ , and  $74 \mu\text{m}$ . The y-axes of Figure 2(b) and Figure 2(c) is the ratio between the back scattered far-field pattern from the cylinder coated with magnetite and the back scattered far-field pattern from the uncoated cylinder. A comparison of Figure 2(b) and Figure 2(c) shows that the TE polarization is more sensitive than the TM polarization in detecting corrosion. For example, a magnetite thickness of  $74 \mu\text{m}$  perturbs the back scattered far-field pattern by a maximum 0.35 % for the TM polarization, whereas it perturbs the back scattered far-field pattern by a maximum of 5 % for the TE polarization in comparison to the uncoated cylinder. Therefore, the results in Figure 2 show that corrosion in the  $3 \mu\text{m}$  to  $74 \mu\text{m}$  thickness range can be detected in the W-band more accurately using the TE polarization. Therefore, in the rest of the cases in this paper only the TE polarization will be presented.

The TE back-scattered far-field pattern from a 1.27 cm diameter cylinder covered with one layer of a packaging tape was measured using the experimental setup previously described. The packaging tape had a thickness of 63.5

$\mu\text{m}$  and, since it is based on propylene, it is assumed that it had a relative dielectric permittivity  $\epsilon_r = 2.4$ . The packaging tape was chosen in this experimental test since it had a thickness comparable to the corrosion thicknesses of interest and because its thickness could be made uniform around the cylinder. The measurements from the uniform packaging tape case are shown in Figure 3. The y-axis of Figure 3 is the ratio between the back scattered far-field pattern from the cylinder coated with the tape to the back scattered far-field pattern from the uncoated cylinder. The numerical simulations of the uniform packaging tape configuration is shown in blue whereas the experimental measurements are shown in red. The same measurement was repeated twice and presented in Figure 3. The difference between the two experimental measurements, a measure of the experimental uncertainty, can be attributed to slight movement or misalignment of the cylinder between the two measurements. Even though the difference between the coated and the uncoated back scattered far-field pattern is on the order of 2 %, both experimental measurements agree very well with the numerical simulations, indicating that coatings with very small thickness can be detected experimentally in the W-band.

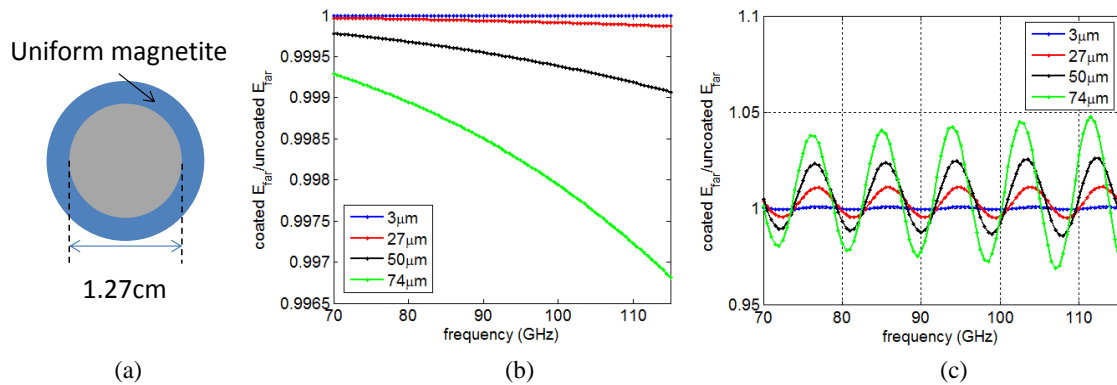


**FIGURE 2.** (a) Configuration of the 1.27 cm diameter metallic cylinder covered with magnetite layers of different thickness (b) Numerical scattered field for the TM polarization (c) Numerical scattered field for the TE polarization.

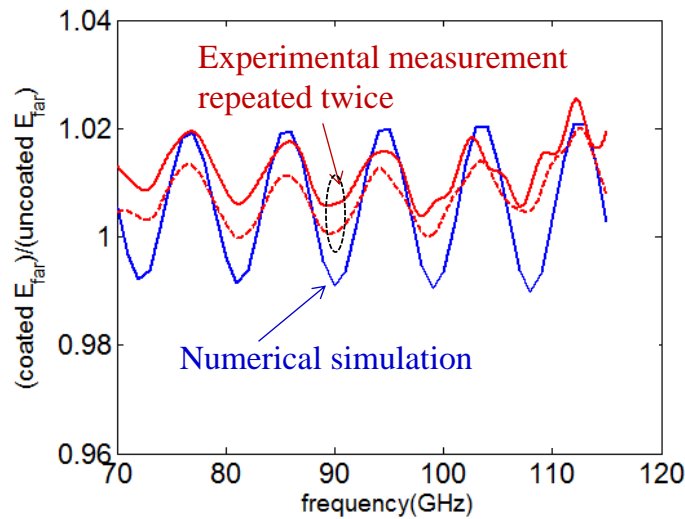


**FIGURE 3.** TE experimental and numerical scattered fields from a 1.27 cm diameter metallic cylinder covered uniformly with one layer of packaging tape.

### Effect of Concrete Thickness

In this section, cylinders with uniform layers of magnetite coating were computationally embedded in dry concrete cylinders of different thickness as shown in Figure 4(a). The dry concrete was selected to be cylindrical in shape to facilitate the use of the fast analytical solutions in [5,6]. This is an unrealistic geometry for rebar in

concrete, but the goal of this subsection is to investigate qualitatively how concrete affects the signature of a magnetite layer in the W-band. The relative dielectric permittivity of dry concrete is estimated to be  $\epsilon_r = 4 - j0.06$  similar to the value reported in [10]. However, the measurements performed in [10] were performed at a maximum frequency of 20 GHz. The dielectric permittivity will vary considerably with concrete moisture content [10].

Two different concrete thickness, 2 cm and 4 cm, were simulated and the results are shown in Figure 4(b) and 4(c), respectively. In both cases, the y-axis represents the ratio of the TE backscattered far-field pattern due to the concrete+magnetite+cylinder to the TE backscattered far-field pattern due to the concrete+ cylinder only. In the case of the 2 cm concrete layer, the signature of the magnetite was around 5 % at most frequencies, which is the same value as the rebar in air. However, at some frequencies it can exceed 10 %, which can be attributed to multiple reflections inside the low-loss relatively thin dry concrete layer, which can enhance the magnetite layer signature. When the concrete thickness doubles to 4 cm, the signature of the magnetite layer drops to a value of around 0.5 %.

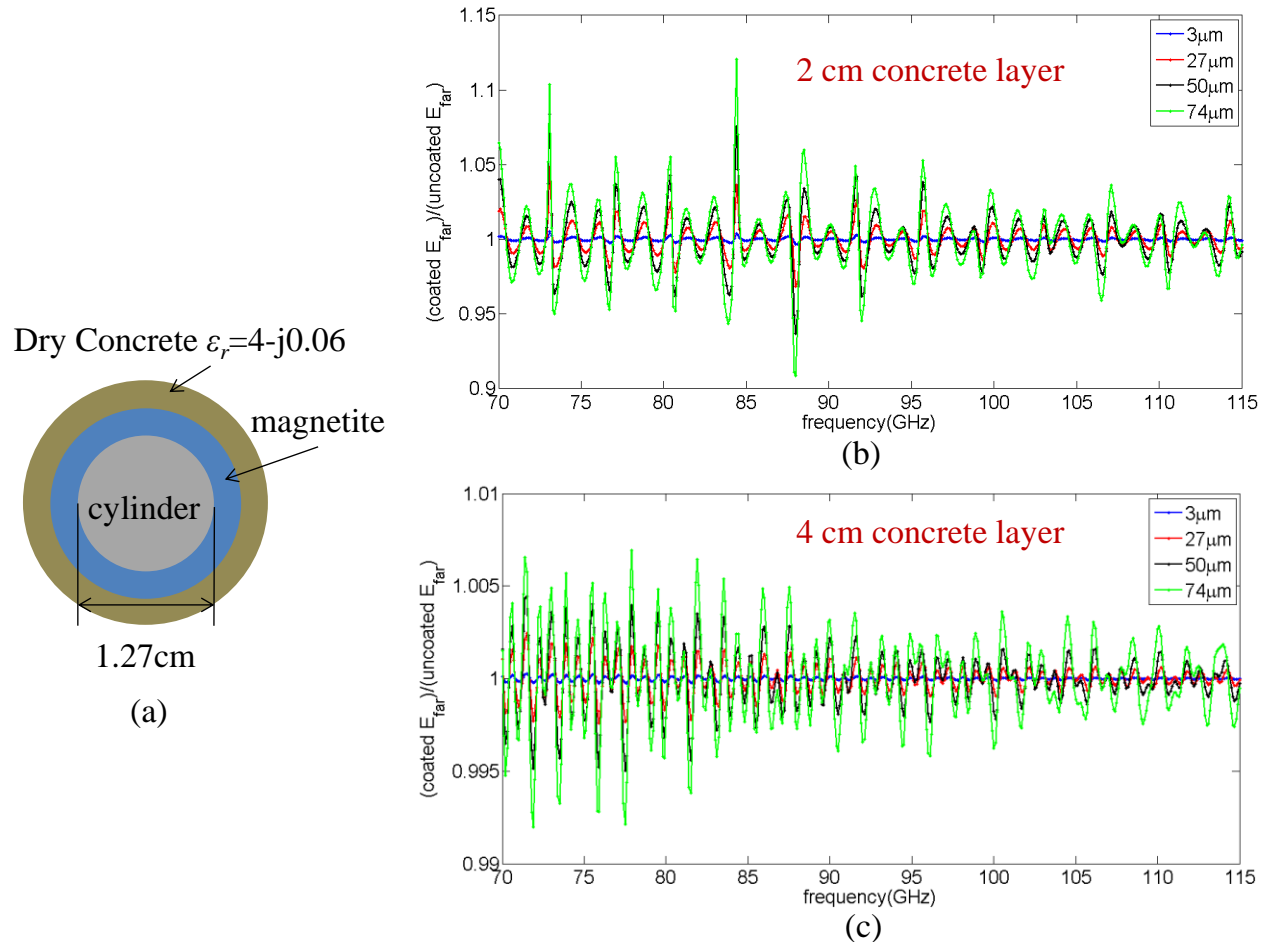


**FIGURE 4.** (a) Configuration of cylinder coated with magnetite and embedded in concrete, (b) TE numerical scattered fields from a 2 cm thick concrete layer, and (c) TE numerical scattered fields from a 4 cm thick concrete layer.

### Effect of Non-uniform Corrosion

Only uniform corrosion layers have been considered in the previous subsections. In this subsection non-uniform corrosion is investigated using tape strips. Tape strips are employed again in this study since their location, angle of coverage and thickness can be easily controlled. In the experimental measurements, a 1.27 cm diameter metallic cylinder was employed. Two horizontal strips of tape were overlapped and adhered to the cylinder as shown in Figure 5(a). Each strip had a thickness of 0.2 mm and, therefore, the overall thickness of the tape layer is 0.4 mm. The tape does not go all around the cylinder. The width of the tape is 2.54 cm and therefore, the horizontal strips

cover only an angle of  $230^\circ$  around the cylinder. In the numerical simulations, the theoretical solutions cannot easily simulate non-uniform coverage. Therefore, the Radio-Frequency (RF) module of the Finite Element commercial COMSOL multiphysics package was employed to calculate the scattered field in the non-uniform coverage case. The exact relative dielectric permittivity of this tape was unknown and, therefore, it is estimated to be  $\epsilon_r = 3$  in the simulations. Different angles of coverage  $\theta$  were simulated using COMSOL as shown in Figure 5(b) to emulate non-uniform corrosion.

Figure 6(a) shows the experimental measurement for a tape covering an angle of  $230^\circ$  and the COMSOL simulations for a tape covering angles of  $180^\circ$  and  $230^\circ$ . The  $y$ -axis of Figure 6(a) is the ratio between the back scattered far-field pattern from the cylinder coated with the tape and the back scattered far-field pattern from the uncoated cylinder, whereas the  $x$ -axis is the frequency in GHz. The experimental and the numerical simulations follow approximately the same envelope. But the experimental measurements show smaller magnitude than the simulations, probably greater than the experimental uncertainty. This can be attributed to uncertainty in the relative dielectric permittivity of the tape. Also the tape in COMSOL is assumed to be in the center of the beam, whereas it can be rotated slightly in the experimental measurements. Figure 6(b) shows the COMSOL simulations for a tape covering angles of  $180^\circ$ ,  $230^\circ$ , and the full coverage angle of  $360^\circ$ . A significant difference between the partial coverage cases of  $180^\circ$  and  $230^\circ$  and the full coverage angle of  $360^\circ$  can be seen in Figure 6(b). The full coverage case shows more frequent resonances with much higher magnitude. This indicates a resonance phenomenon that only occurs in the case of full coverage.

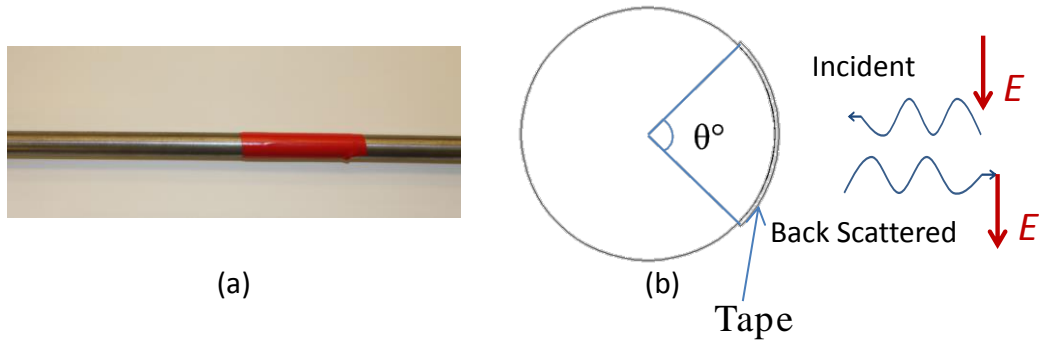


**FIGURE 5.** The configuration of the non-uniform coverage employed in the (a) experimental measurements and (b) COMSOL numerical simulations

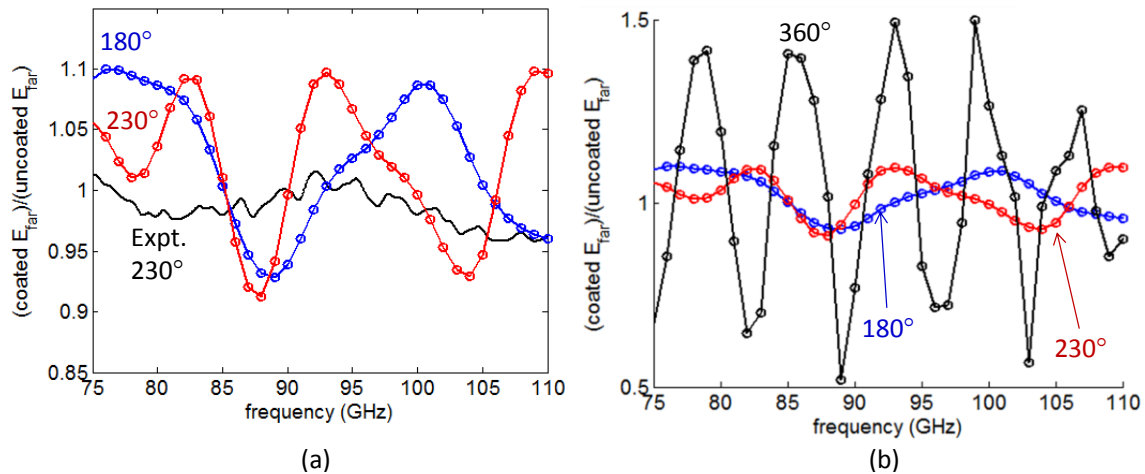


**FIGURE 6.** (a) Experimental and numerical scattered fields from non-uniform coatings and (b) numerical scattered fields from non-uniform coatings of different coverage angles

## Effect of Rebar Surface Geometry

Rebar typically has ribs or thread to improve adhesion to the concrete matrix. An example of these ribs or threads is shown in Figure 7(a). The heights of these ribs are of the order of a few millimeters, which are much smaller than microwave wavelengths. However, in the W-band these rib dimensions are comparable to the wavelength and, therefore, their effect has to be specifically investigated. The scattered fields from the complex surface geometry in real rebar cannot be simulated theoretically and, therefore, COMSOL is utilized. The rebar is assumed to be free of corrosion and of infinite length by modeling a unit cell of rebar and imposing periodic boundary conditions in the z-axis to extend this unit cell to infinity. Figure 7(b) shows the COMSOL unit cell of rebar. Figure 7(c) shows the backscattered far-field pattern for a cylinder with or without the ribs. At low frequencies, up to 10 GHz, the effect of the ribs or threads is minimal but as the frequency increases the backscattered field diverges greatly between the two cases. Figure 7(d) focuses on the W-band and compares the experimental measurements and the COMSOL simulations from rebar, which are in reasonable agreement. Figure 7(d) shows significance difference between the backscattered far-field pattern from rebar and the backscattered far-field pattern from cylinders. Therefore, for the accurate NDE of corrosion in rebar, the surface geometry of rebar probably needs to be accurately modeled.

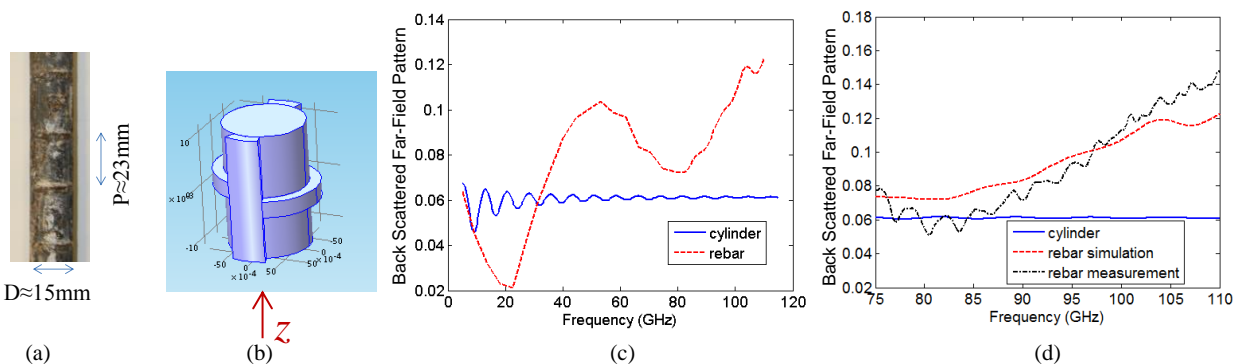


**FIGURE 7.** (a) Photograph of rebar, (b) COMSOL model of a rebar unit cell, (c) Numerical simulation of the TE back scattered far-field pattern from rebar with and without ribs in the microwave/millimeter wave bands, and (d) Experimental measurements and numerical simulation of the TE back scattered far-field pattern from rebar with and without ribs in the W-band

## CONCLUSIONS AND FUTURE WORK

An experimental setup was developed for the NDE of cylinder and rebar in the W-band. The experimental measurements compared favorably with numerical simulations for a variety of configurations, validating that a plethora of information can be extracted from back scattered fields in the W-band. The experimental measurements and simulations were utilized to investigate different configurations of corrosion product layers. The TE polarization was found to be more sensitive than the TM polarization in detecting geometrical changes. Also, the amplitude and structure of the signature of a magnetite layer was explored as a function of concrete layer thicknesses up to a maximum of 4 cm. Future work will investigate the effect of different rebar surface geometries since the ribs and threads were found to strongly impact the scattered fields. The effect of local geometry on the AFMR resonance will also be investigated.

## ACKNOWLEDGMENTS

This work is funded by the NIST Innovations in Measurement Science (IMS) project, “Detection of Corrosion in Steel-Reinforced Concrete by Antiferromagnetic Resonance.”

## REFERENCES

1. G. Roqueta, L. Jofre, and M. Feng, *IEEE Transactions on Instrumentation and Measurements*, **61**, 1090-1098, (2012).
2. S. Kim, J. Surek, and J. Baker-Jarvis, *Journal of Research of the National Institute of Standards and Technology*, **116**, 655-669, (2011).
3. S. Chou, P. Stutzman, S. Wang, E. Garboczi, W. Egelhoff, and D. Plusquellic, *J. Phys. Chem. C*, **116**, 16161–16166, (2012).
4. E.J. Garboczi, P.E. Stutzman, S. Wang, N.S. Martys, D. Duthinh, V. Provenzano, S.G. Chou, D.F. Plusquellic, J. Surek, S. Kim, R.D. McMichael, and M.D. Stiles, QNDE 2013 proceedings, Baltimore, MD, 2013.
5. C. Tang, *Journal of Applied Physics*, **28**, 628-633, (1957).
6. T. Rao and M. Hamid, *International Journal of Electronics*, **38**, 667-673, (1975).
7. S. Kozaki, *IEEE Transactions on Antennas and Propagation*, **30**, 881-887, (1982).
8. P. Goldsmith, *Quasioptical Systems: Gaussian Beam Quasioptical Propagation and Applications*, Wiley-IEEE Press, 1998.
9. S. Kim, J. Surek, J. Baker-Jarvis, and V. Provenzano, *Proceedings of the 2012 Conference on Precision Electromagnetic Measurements (CPEM)*, Washington DC, 2012, pp. 640-641.
10. H. Rhim and O. Büyükoztürk, *ACI Materials Journal*, pp. 262-271, 1998.